ACS NANO

Subscriber access provided by Argonne Research Library

Article

Quantitative Three Dimensional Characterization of Block Copolymer Directed Self -Assembly on Combined Chemical and Topographical Pre-Patterned Templates

Tamar Segal-Peretz, Jiaxing Ren, Shisheng Xiong, Gurdaman Khaira, Alec Bowen, Leonidas E. Ocola, Ralu Divan, Manolis Doxastakis, Nicola J. Ferrier, Juan J. de Pablo, and Paul F Nealey

ACS Nano, **Just Accepted Manuscript** • DOI: 10.1021/acsnano.6b05657 • Publication Date (Web): 22 Dec 2016

Downloaded from http://pubs.acs.org on January 3, 2017

Just Accepted

"Just Accepted" manuscripts have been peer-reviewed and accepted for publication. They are posted online prior to technical editing, formatting for publication and author proofing. The American Chemical Society provides "Just Accepted" as a free service to the research community to expedite the dissemination of scientific material as soon as possible after acceptance. "Just Accepted" manuscripts appear in full in PDF format accompanied by an HTML abstract. "Just Accepted" manuscripts have been fully peer reviewed, but should not be considered the official version of record. They are accessible to all readers and citable by the Digital Object Identifier (DOI®). "Just Accepted" is an optional service offered to authors. Therefore, the "Just Accepted" Web site may not include all articles that will be published in the journal. After a manuscript is technically edited and formatted, it will be removed from the "Just Accepted" Web site and published as an ASAP article. Note that technical editing may introduce minor changes to the manuscript text and/or graphics which could affect content, and all legal disclaimers and ethical guidelines that apply to the journal pertain. ACS cannot be held responsible for errors or consequences arising from the use of information contained in these "Just Accepted" manuscripts.

ACS Publications

ACS Nano is published by the American Chemical Society. 1155 Sixteenth Street N.W., Washington, DC 20036

Published by American Chemical Society. Copyright © American Chemical Society. However, no copyright claim is made to original U.S. Government works, or works produced by employees of any Commonwealth realm Crown government in the course of their duties.

Quantitative Three Dimensional Characterization of Block Copolymer Directed Self -Assembly on Combined Chemical and Topographical Pre-Patterned Templates

Tamar Segal-Peretz,[1,2,3*] Jiaxing Ren,[1,2*] Shisheng Xiong,[1] Gurdaman Khaira,[1] Alec Bowen,[1] Leonidas E. Ocola,[4] Ralu Divan,[4] Manolis Doxastakis,[1] Nicola J. Ferrier,[5] Juan de Pablo,[1,2] and Paul F. Nealey.[1,2]

[1] Institute for Molecular Engineering, University of Chicago, 5640 South Ellis Ave, Chicago, 60637, United States
[2] Materials Science Division, Argonne National Laboratory, 9700 S. Cass Avenue, Argonne, Illinois 60439, United States
[3] Department of Chemical Engineering, Technion- Institute of Technology, Haifa 3200003, Israel
[4] Center for Nanoscale Materials, Argonne National Laboratory, 9700 S. Cass Avenue, Argonne, Illinois 60439, United States
[5] Mathematics and Computer Science Division, Argonne National Laboratory, 9700 S. Cass Avenue, Argonne, Illinois 60439, United States

* - these authors contributed equally to this work

Corresponding author: nealey@uchicago.edu

Graphical abstract:

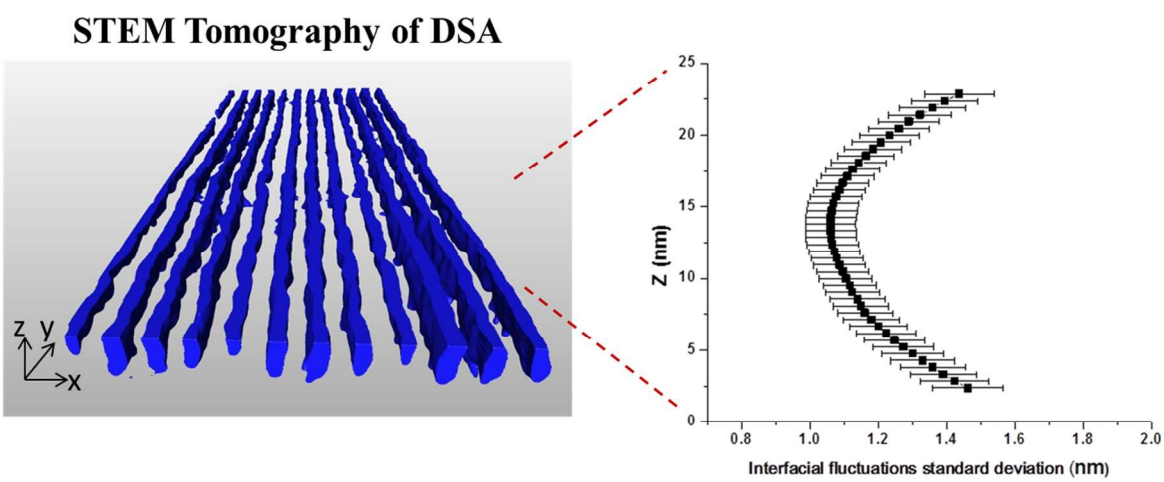

Abstract

Characterization of the three-dimensional (3D) structure in directed self-assembly (DSA) of block copolymers is crucial for understanding the complex relationships between the guiding template and the resulting polymer structure so DSA could be successfully implemented for advanced lithography applications. Here we combined scanning transmission electron microscopy tomography and coarse-grain simulations to probe the 3D structure of P2VP-*b*-PS-*b*-P2VP assembled on pre-patterned templates using solvent vapor annealing. The templates consisted of non-preferential background and raised guiding stripes that had PS-preferential top surfaces and P2VP-preferential sidewalls. The full 3D characterization allowed us to quantify the shape of the polymer domains and the interface between domains as a function of depth in the film and template geometry and offered important insights that were not accessible with 2D metrology. Sidewall guiding was advantageous in promoting the alignment and lowering the roughness of the P2VP domains over the sidewalls; but incommensurate confinement from the increased topography could cause roughness and intermittent dislocations in domains over the background region at the bottom of the film. 3D characterization of bridge structures between domains over the background and breaks within domains on guiding lines sheds light on possible origins of common DSA defects. The positional fluctuations of the PS/P2VP interface between domains showed a depth-dependent behavior, with high levels of fluctuations near both the free surface of the film and the substrate, and lower fluctuation levels in the middle of the film. This research demonstrates how 3D characterization offers a better understanding of DSA processes, leading to better design and fabrication of directing templates.

Key words: block copolymer, directed self-assembly, TEM tomography, fluctuations, defects, P2VP-*b*-PS-*b*-P2VP.

In recent years, as the feature size in nanomanufacturing has scaled down into the sub-20 nm regime, approaches such as self-aligned double and quadruple pattering,[1-3] and directed self-assembly (DSA) of block copolymers (BCP)[4-5] were developed in order to extend patterning capabilities beyond the resolution limits of conventional optical lithography tools. In all these processes, there is a need for tight control over the feature size, the feature's three-dimensional (3D) profile, and over the fluctuation of the feature's size and shape to meet stringent manufacturing constraints for semiconductors. Probing and understanding the three-dimensional morphology of the pattern is therefore important for the development of new materials and processes in nanomanufacturing.

In DSA, BCPs are directed to assemble by chemical or topographical pre-pattern templates in a bottom-up process.[4, 6] Thus, probing the 3D morphology of BCP DSA is necessary not only for determining the exact structure of the DSA film, but to enable better understanding of the relationship between the guiding pattern and the final assembled film. In general, the final 3D morphology of a DSA film is determined by the BCP chemistry, together with the guiding pattern geometry and chemistry, and the processing conditions.[6-7] It's therefore desirable to obtain a detailed correlation between all these parameters and the DSA film morphology.

Besides controlling the through-film morphology and the features' fluctuations, DSA films should also exhibit defectivity levels that are compatible with the semiconductor industry (~1 defect per 100 cm^2 area) in order to be implemented in manufacturing. To achieve this low defectivity level, the origins of DSA defects should be better understood.[8-10] However, optical metrology tools and scanning electron microscopy (SEM), which are routinely used for defect detection and process window evaluation, cannot detect defects which are hidden underneath the BCP surface and might over predict the process window.[11-12] These defects often become apparent only after the pattern transfer process, and tracing their origin is challenging since both the BCP layer and the pattern transfer process can contribute to its formation. Indeed, both Gronheid *et al.*[12] and Wan *et al.*[13] reported that defects which were not identified after BCP DSA, appeared at the end of the pattern transfer process. Thus, probing the local BCP structure in 3D assists in identifying hidden defects, while mapping their 3D structure can shed light on their origin.

Two main 3D characterization techniques of BCP thin films have been demonstrated in the last few years. The first is based on reciprocal space characterization using X-ray scattering demonstrated by Stein *et al.*[14] and by Sunday *et al.*[15-16] X-ray scattering is a powerful technique which probes large-area samples with sub-nm resolution. It relies on high intensity scattering from periodic features, providing valuable statistical information on the average structure and fluctuations in structure from macroscopic areas. However, X-ray scattering requires a model to derive the structure from reciprocal space data, and provides limited information about individual BCP features and non-periodic structures such as defects. The second 3D characterization technique is based on real space characterization using transmission electron microscope (TEM) tomography. Although sampling size is limited in TEM, it is considered a powerful technique for BCP DSA metrology,[17] providing the data necessary for understanding BCP assembly in 3D,[18-19] for studying defect formation,[9, 19] and for validating molecular simulations.[18-19] The relatively straight-forward interpretation of TEM tomography data, and recent progress in sample preparation,[17] make it an attractive method for probing the structure BCP DSA films. Moreover, since TEM tomography is a real-space characterization method, it is possible to decouple the average shape of the structure (in the field of view) from the positional fluctuation of the shape, and measure them independently.

Here we develop in-depth understanding of the through-film structure, fluctuation in structure, and defects in DSA films of high-χ (Flory-Huggins interaction parameter), solvent vapor annealed (SVA), poly(2-vinylpyridne)-*b*-polystyrene-*b*-poly(2-vinylpyridne) (P2VP-*b*-PS-*b*-P2VP) triblock copolymer, through scanning TEM (STEM) tomography and theoretically informed coarse-grain (TICG) simulations results. SVA is known to mitigate the differences in interfacial energies at the film's free surface and enable sub-10 nm DSA,[20-26] while P2VP-*b*-PS-*b*-P2VP has high χ (0.18 at room temperature),[27-28] and was recently shown to be directed into highly ordered patterns.[21, 24, 26, 29] The effect of the template's dimensions on the 3D BCP structure was investigated by systematically changing the width of the guiding stripes from 0.7 $L_{0,s}$ to 1.9 $L_{0,s}$ in 4x density multiplication pre-pattern pattern, where $L_{0,s}$ is self-assembled period of the polymer after undergoing the SVA process. A combination of tomographic characterization and TICG simulations revealed that two regimes of guide stripe width lead to aligned assembly at the top of the film. However, the internal BCP structure in these regimes is significantly different in terms of assembly on the top and sides of the cross linked polystyrene

(X-PS) guiding stripes, the curvature of the assembled lamellae in the through-film structure, and the defect levels at the BCP-template interface. The 3D characterization also showed that the topography of the pre-pattern template plays a strong role in the assembly in terms of the level of alignment and defect formation. Analysis of the fluctuation of the interface between PS and P2VP domains revealed that the interface positional fluctuation depends on the location of the domains with respect to the underlying template and on the distance away from the free surface of the film and the substrate. Moreover, by quantifying the 2D shape of the domains and their positional fluctuations, we were able to probe the compositional profile of the domain interface. Finally, STEM tomography characterization enabled us to probe the 3D structure of common defects such as micro-bridge defect and line breakage defects, giving insights to their origins.

Results and discussion:

BCP DSA for 3D characterization

Samples were prepared for TEM imaging and tomography according to the procedure illustrated in Figure 1. Detailed description can be found in the experimental section and in previous reports.[17] In short, 4" SiN_x/Si/SiN_x (30 nm/200 μm/30 nm) wafers were patterned on the back side using optical lithography to define openings in the back SiN_x that would later serve as an etching mask to create individual SiN_x windows. Then, templates consisting of X-PS mats and hydroxyl terminated polystyrene brushes (PS-OH) were fabricated using the Liu-Nealey (LINE) flow on the front side of the SiN_x/Si/SiN_x wafer (Figure 1a).[7] The X-PS guiding stripes were fabricated using ebeam lithography and oxygen-plasma etch. The etch processes exposes the X-PS sidewalls to oxygen plasma, leading to different chemistry between the sidewalls and top surface of the X-PS guide stripes.[30] The oxidized sidewalls of the guide stripes were preferential for the more polar block of the polymer, in this case P2VP, and the protected top surface was preferential for PS. Low molecular weight (1.2k) PS-OH brush, which has been shown to induce P2VP-*b*-PS-*b*-P2VP perpendicular domains in self-assembly films (Figure S1, supporting information), was grafted on the exposed substrate sections, and presumably and to a lesser extent to the X-PS sidewalls. The modified sidewalls remained P2VP preferential and together with the non-preferential background and PS preferential guide stripe formed a three-tone chemistry. The period ($L_{0,s}$) of P2VP-*b*-PS-*b*-P2VP in the solvated but micro-phase separated state under the SVA conditions used in this study was 21.3 nm, as determined by

grazing incident small angle X-ray (GISAXS) measurement of SVA self-assembled films (Figure S2, supporting information). Therefore, the pitch of the template (L_s) was designed to be 84 nm, for DSA with 4 X density multiplication. In addition, the templates had ~ 5 nm topography (~ 0.25 $L_{0,s}$), with ~ 7 nm thick X-PS guiding stripes, and ~ 2 nm thick PS-OH brush background. The role of topography in template will be discussed in the following section. To study the effect of the template geometry on the 3D structure of BCP film, the guiding stripe width, W, was varied between 1.9 $L_{0,s}$ and 0.7 $L_{0,s}$ by changing the exposure dose. The geometry of the X-PS guiding stripes was determined after photoresist removal using atomic force microscopy (AFM) measurements (Figure S3, supporting information).

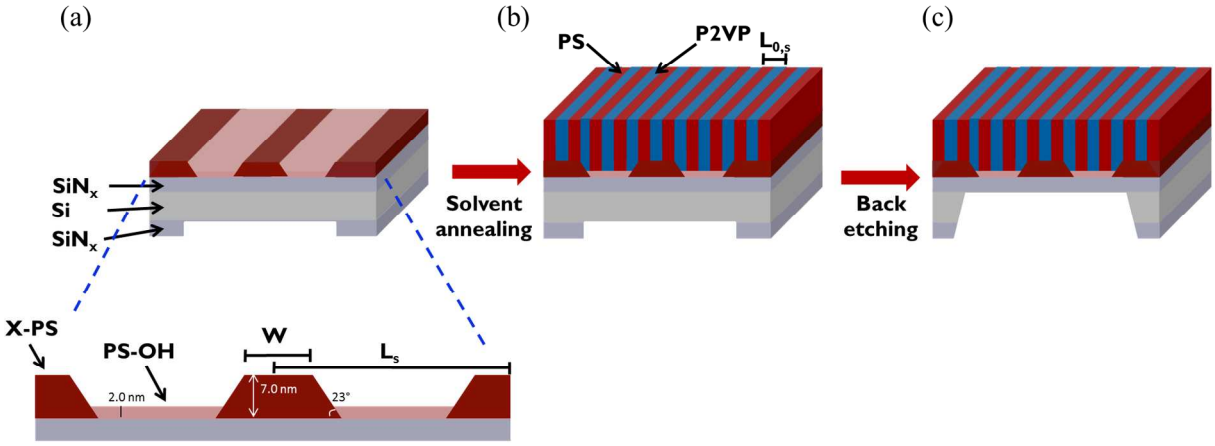

Figure 1: Schematic illustration of sample preparation process. (a) Pre-pattern templates were fabricated on SiN_x/Si/SiN_x 4" wafer. (b) P2VP-*b*-PS-*b*-P2VP was directed self-assembled on the templates using acetone solvent vapor annealing. (c) The silicon wafer was back etched to create windows for TEM imaging.

Following the template fabrication, 25 nm thick P2VP-*b*-PS-*b*-P2VP film was spin cast on the wafer and annealed using acetone SVA for 60 min (Figure 1b). Acetone is considered a non-selective solvent to both PS and P2VP blocks, and therefore it mitigates the difference in surface energies between the blocks during the SVA process, enabling assembly of perpendicularly oriented lamellae.[24, 26] The swelling ratio of the polymer film ((swollen film thickness- non-swollen thickness)/ non-swollen thickness) was kept at 42 % during the SVA process and was returned to ~2 % during the rapid drying step. Under these conditions, the BCP assembles in the highly mobile solvated but micro-phase separated state.[26] The solvated PS and P2VP blocks

recognize the template chemistry and topography, leading to well-aligned morphologies.[20] Swelling is not expected to affect the template topography as the X-PS guide stripes were highly crosslinked and the background brush was very thin (2 nm). Upon rapid solvent removal, the domains shrink in the direction normal to the substrate and retain their lateral dimensions in the plane of the film.[31] Following the DSA, the silicon substrate was back etched through the openings defined on the back side using KOH wet etching procedure for ~ 2 hours, forming 200 μm x 1mm windows of BCP/ SiN_x windows (Figure 1c).

Before TEM imaging, samples were stained for 2 hours using iodine vapors. Iodine forms a complex with the P2VP pyridine group, enhancing electron scattering from the P2VP domains.[32] Although the kinetics of iodine staining is unknown, our experience suggests that 2 hours of staining of 25 nm thick film could reach staining saturation. *i.e.* all the available pyridine groups are stained.

Through-film structure of BCP DSA films

In order to decipher the three dimensional morphology, STEM tomography characterization was performed. For each sample, a tilt series of 51 images with tilt angles ranging from -68° to +68° was acquired, followed by alignment and reconstruction, resulting in a reconstructed volume of roughly 850 nm x 850 nm x 40 nm (*x,y,z*). Visualization of the reconstructed volume of P2VP-*b*-PS-*b*-P2VP DSA films on the templates with varying X-PS guide stripes width are shown at high magnification in the left column of Figure 2; low magnification images can be found in Figure S4, supporting information. For clarity, P2VP domains in the visualization images are colored in blue while PS domains are transparent. Corresponding *xy* slices, parallel to the substrate, from close to the top of the film ($z \approx 22$ nm), and close to the bottom of the film ($z \approx 5$ nm) obtained from the reconstructed volumes are shown in the central column. Bright domains in the STEM images correspond to iodine-stained P2VP domains and will be referred to as P2VP domains, while dark domains correspond to PS domains. To quantify the through-films morphology in the films, each reconstructed volume was digitally sliced to 0.48 nm thick *xz* cross sections (the number of cross section varied between 1700 and 1900, according to the size of the reconstructed volume). The individual cross sections from each volume were averaged along the *y* direction to obtain high signal to noise images. An example of such slicing can be found in Movie 1 (supporting information) for P2VP-*b*-PS-*b*-P2VP DSA film on template with

W=1.4 $L_{0,s}$. The averaged cross sections are presented in Figure 2 on the right column together with an illustration of a single X-PS guide stripe (in dark red) to assist the interpretation of the data.

The tomographic data shows that the degree of alignment changes with the width of the guiding stripes. Two regimes (processes windows) of aligned assembly can be identified: the first is around W = 1.5 $L_{0,s}$, where templates with W = 1.6 $L_{0,s}$ and W = 1.4 $L_{0,s}$ direct the BCP into aligned lamellae (Figures 2b and 2c, respectively). In this regime, three lamellae assemble on the top of the guiding stripe (two PS lamellae and one P2VP lamellae), while the X-PS side walls are wetted by P2VP lamellae, as can be seen in the averaged cross sections. Templates with wider X-PS guiding stripes (W = 1.9 $L_{0,s}$) or narrower X-PS guiding stripes (W = 1.1 $L_{0,s}$) result in a non-aligned morphology (Figures 2a and 2d, respectively). The second regime of aligned assembly was identified in templates with X-PS guiding stripes width of 0.8 $L_{0,s}$ and 0.7 $L_{0,s}$ (Figures 2e and 2f, respectively). In this regime, only one PS lamellae assembles on the top of the guiding stripe and the adjacent P2VP lamellae assemble on the X-PS side walls. Similar regimes were also seen in the assembly of PS-*b*-poly methyl methacrylate (PS-*b*-PMMA) on pre-pattern templates.[33]

The tomographic characterization probes the detailed 3D structure of each assembled film. When the X-PS width is tuned to 1.6 $L_{0,s}$ and 1.4 $L_{0,x}$, vertical through-film domains are obtained (Figures 2b and 2c). The *xy* slices (central column) and the full *xy* slice series of P2VP-*b*-PS-*b*-P2VP DSA film on template with W=1.4 $L_{0,s}$ (Movie 2, supporting information) show that one lamella in every four P2VP lamellae "disappears" towards the bottom of the film. Thus, while at the top of the film (Figure 2b and 2c, central column, $z \approx 22$ nm), and through most of the film thickness there are four lamellae in every template pitch (L_s), only three lamellae are seen in each L_S near the BCP-template interface (Figure 2b and 2c, central column, $z \approx 5$ nm). The origin of this assembly is the topography of the template, where the ~ 5 nm difference in height between the X-PS guide stripe and the PS-OH brush results in height variation in the assembly of the lamellae according to their location. The template topography creates two P2VP lamellae populations: P2VP lamellae that assembled on top of the X-PS guiding stripe ($P2VP_G$), and P2VP lamellae that assembled on the PS-OH brush or on the PS-OH brush-PS guide stripe interface ($P2VP_B$, Figure 2b and 2c, right column). Measurements of the *z* length of each

population in the averaged cross section (Figure 2c, right column) corroborate that there is ~ 5 nm *z* length difference between the two populations. The two lamellae populations also differ in their brightness intensity; in both the single cross sections and in the averaged cross sections, $P2VP_G$ has lower brightness than $P2VP_B$. This was attributed to lower scattered electron detection by the annular STEM detector due to the X-PS that is present below the $P2VP_G$.

When the width of the X-PS is tuned to W=1.9 $L_{0,s}$ and W=1.1 $L_{0,s}$, non-aligned lamellae are assembled due to the mismatch between W and BCP domain size (Figure 2a and 2d). Interestingly, even near the interface with the brush domain, where there is geometrical constraint of the X-PS guide stripes, the lamellae are still non-aligned or only partly-aligned, as can be seen in Figure 2a and 2d – central column, $z \approx 5$ nm. The non-aligned assembly results in blurred averaged cross sections (Figures 2a and 2d, right column) due to the variety of orientations of the BCP. The difference in blurriness within these cross sections corresponds to the percentage of misalignment in the particular area where the tomography and averaging were performed.

When W is further decreased to 0.8 $L_{0,s}$, aligned assembly is obtained but the films had higher defect levels than what was observed in the first aligned regime (Figures S5 and S6, supporting information). In this regime, the tomographic characterization reveals an interesting phenomenon; while aligned lamellae are seen at the top of the film (Figure 2e, central column, $z \approx 22$ nm) and this assembly would probably be deemed as satisfactory aligned assembly in top-down imaging, there is significant deviation between the assembly at the top and the assembly at the bottom of the film; many defects appear close to the interface the BCP and the brush (Figure 2e, central column, $z \approx 5$ nm), and curved lamellae are observed in the averaged cross section (Figure 2e, right column). These defects are formed at the bottom 5 nm of the film, between the X-PS guide stripes, as can be seen from the full *xy* slice series (Movie 3, supporting information). Assembly directed by templates with W=0.7 $L_{0,s}$ showed similar behavior (Figure 2f), and the differences between the two morphologies will be discussed shortly. Despite the defects at the bottom of the film, averaged cross sections show uniform structures along the *y* axis (Figures 2e and 3f, right column, respectively). These averaged cross sections reveal a significant difference between the two P2VP lamellae populations in these films: the external P2VP lamellae in the L_s repeating unit (P2VP-side; $P2VP_S$) and the two central lamellae in the L_s

repeating unit (P2VP-center; $P2VP_C$). At the top two thirds of the film, all lamellae form perpendicular morphology. However, at the bottom third of the film thickness, $P2VP_s$ curve and become narrower at the brush-BCP interface, while $P2VP_C$ remain relatively straight and with constant width. Comparison between the assemblies at W=0.8 $L_{0,s}$ and W=0.7 $L_{0,s}$ shows that the curvature of $P2VP_S$ is dependent on the template's geometry. While $P2VP_C$ are straight in both cross sections, the curvature of $P2VP_S$ is larger in the assembled film with W=0.8 $L_{0.s}$ (Figure 2e, right column) compared to the assembled film with 0.7 $L_{0,s}$ (Figure 2f, right column).

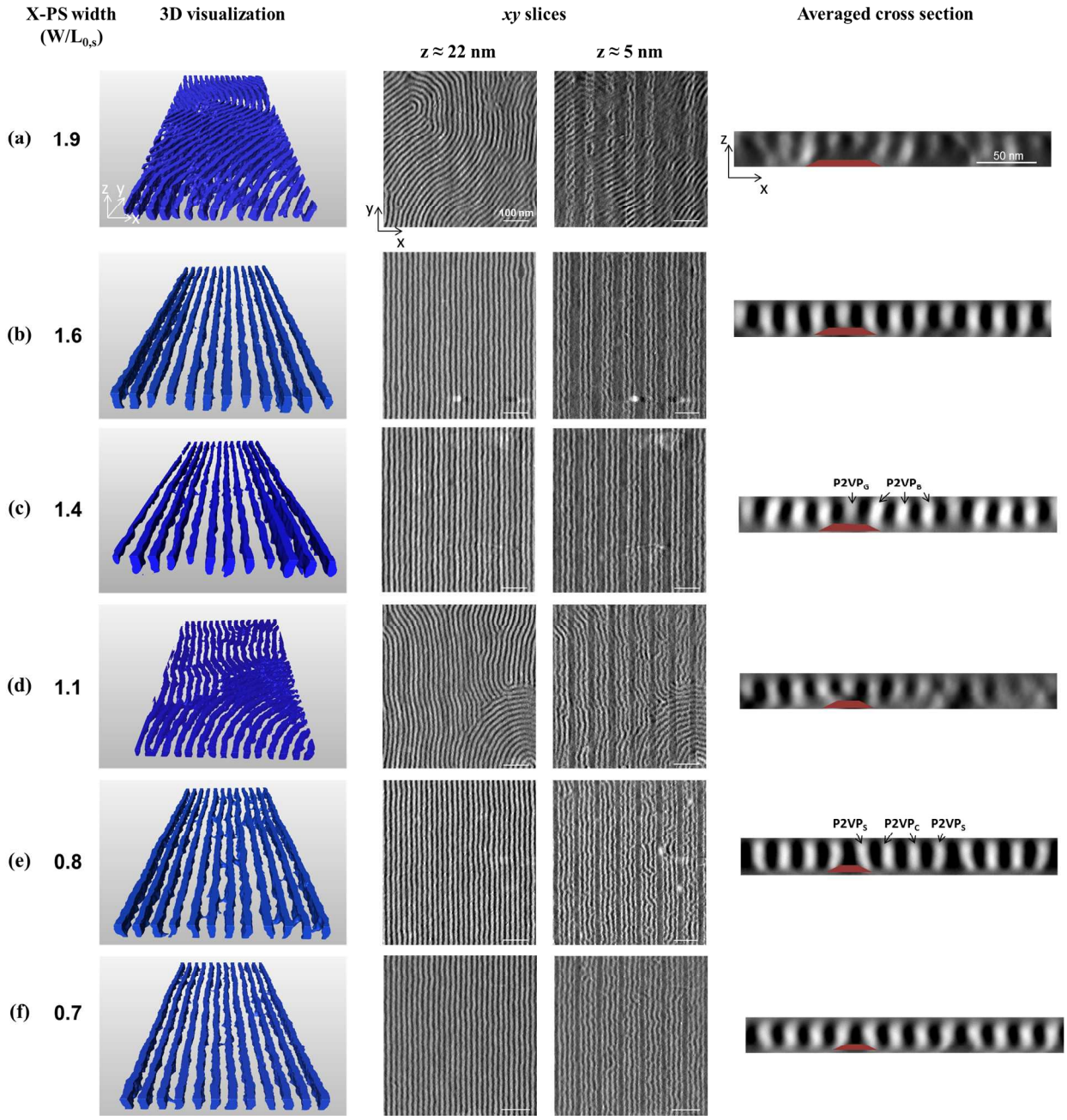

Figure 2: STEM tomography data of P2VP-*b*-PS-*b*-P2VP DSA film on pre-pattern templates with varying X-PS guide stripes width: high magnification visualization of the reconstructed volume (left column), 0.48 nm thick, parallel to the substrate (*xy*), slices of the reconstructed volume taken close to the top of the film (z ≈ 22 nm, central column on the left), and close to the bottom of the film (z ≈ 5 nm, central column on the right), and averaged cross sections of the reconstructed volume (right column). P2VP domains in the 3D reconstructed volume visualization are colored in blue while PS domains are transparent. One X-PS guide stripe is illustrated in each cross section to highlight the location of the pre-pattern template.

Several conditions could have contributed to the defects formation and the thin, curved, lamellae observed at the bottom of the film. First, the preferred wetting of the side walls by P2VP together with the width of the brush regions of the template imposed a spatial constraint on the assembly, *i.e.* the brush region was not wide enough to accommodate four P2VP and three PS lamellae. Indeed, when the brush region was wider at W=0.7 $L_{0,s}$, the curvature of $P2VP_S$ was reduced. Second, a gradient in the solvent evaporation during the drying step in the SVA process could have created volume fraction constraints that can lead to thin P2VP domains where there is preferred wetting (X-PS sidewalls). We anticipate that if W were decreased to 0.5 $L_{0,s}$, the $P2VP_S$ curvature would be further decreased and non-defective, perpendicular and aligned lamellae would be assembled.

Importantly, the effect of the morphologies seen in Figures 2e and 2f on the pattern transfer of the BCP film has not been explored yet. There is a concern that these BCP patterns will be categorized as aligned assembly by top-down meteorology tools but would lead to defective lines after the pattern transfer process. In addition, placement errors and variation in pattern width can occur due to the curved lamellae at the bottom of the film.

To gain insight into the BCP-template interactions and to quantify their role in DSA, TICG simulations were performed. Figures 3a and 3b show TICG simulations of P2VP-*b*-PS-*b*-P2VP DSA films on template patterns with different interaction chemistries (W=1.4 $L_{0,s}$, in both simulations). The template in Figure 3a was modeled as a two-tone pre-pattern template where the X-PS guide stripes are preferential to PS wetting uniformly across both top and sides of the guiding stripe. The strength of interaction, $\Lambda_s N$, was set to -0.5 ($\Lambda_{top}N = \Lambda_{side}N = -0.5$) according to a series of simulations (Figure S7, supporting information) and previous templates models.[34-35] The brush wetting was modeled to be non-preferential ($\Lambda_{brush}N = 0$). This simulated template leads to non-aligned assembly (Figure 3a). Simulating the assembly using a three-tone template, on the other hand, resulted in highly aligned assembly (Figure 3b), in good agreement with the experimental results (Figure 2c). In the three-tone pattern, the top of the X-PS was modeled to be slightly preferential to PS ($\Lambda_{top}N = -0.5$), while the sides of the guide stripes were modeled to be preferential for P2VP wetting with higher strength of interaction ($\Lambda_{side}N = 1.0$), creating three distinctive zones for guiding the assembly. The variation in wetting between the three zones of

the template seen here is in good agreement with recent reports on three-tone templates for PS-*b*-PMMA and other BCPs.[30, 36]

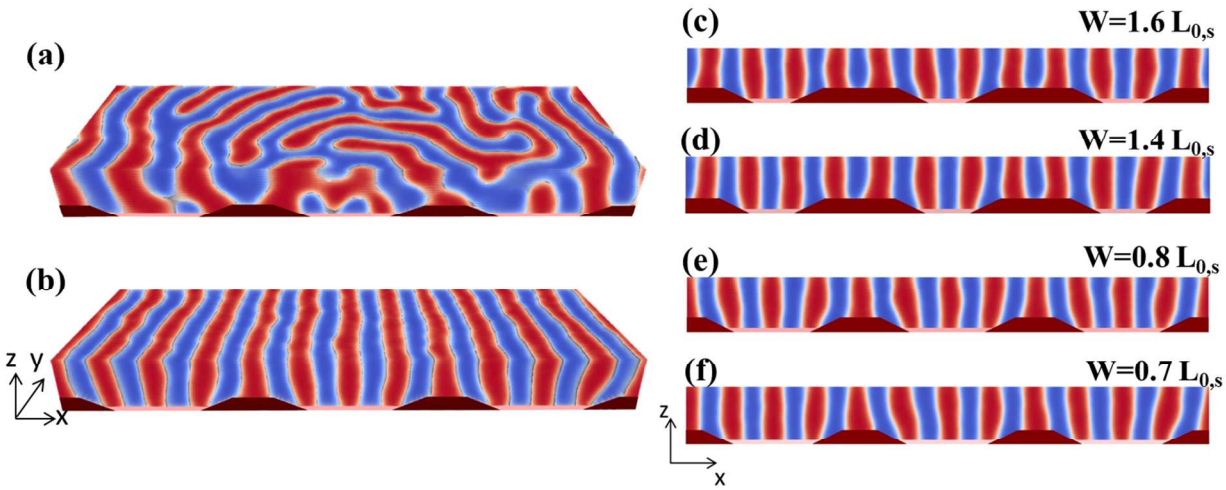

Figure 3: (a,b) TICG simulations of P2VP-*b*-PS-*b*-P2VP DSA films on templates with W=1.4 $L_{0,s}$ with different interaction geometry: (a) the pre-pattern template has two-tone interaction with the BCP ($\Lambda_{top}N=\Lambda_{side}N=-1.0$; $\Lambda_{brush}N=0$), and (b) the pre-pattern template has three-tone interaction with the BCP ($\Lambda_{top}N=-0.5$; $\Lambda_{side}N=1.0$; $\Lambda_{brush}N=0$). (c-f) TICG simulations of P2VP-*b*-PS-*b*-P2VP DSA films on pre-pattern templates with three-tone interaction geometry with varying X-PS guide stripes width. Blue domains correspond to P2VP domains, red domains correspond to PS domains, while the white domains correspond to PS-P2VP interface.

The quantification of the BCP-template interactions enabled us to examine this interface in the DSA films. Templates that resulted in aligned morphology in the experimental set up (W=1.6 $L_{0,s}$, 1.4 $L_{0,s}$, 0.8 $L_{0,s}$, and 0.7 $L_{0,s}$, Figures 2b, 2c, 2e, and 2f, respectively) were modeled using TICG simulations (Figures 3c-3f). The good agreement between the molecular simulations and the tomographic results corroborates the three-tone model and highlights the role of the template's chemistry and topography in creating a side-wall driven (or assisted) directed assembly. In addition, the simulations shed light on the origin of curvature in $P2VP_S$ in the assemblies with W=0.8 $L_{0,s}$ and W=0.7 $L_{0,s}$ (Figures 3e and 3f, respectively). The favorable interaction of the X-PS side walls with the P2VP domains leads to assembly where the P2VP follow the geometry of the X-PS guide stripe side walls, which results in curved lamellae near the interface with the guide stripe. Indeed, the simulations show that the P2VP curvature decreases with decreasing guide stripe width, in good agreement with the tomographic results (Figures 2e and 2f).

Fluctuations and interfacial width

To fully explore a DSA system, it is necessary to probe both the through-film structure *and* the positional fluctuations in shape, size and placement of the structures with respect to the underlying template. The local interface between two domains in a BCP system is a diffuse interface with a finite interfacial width, Δ, over which the composition normal to the plane of the interface changes from A to B, and is well-modeled by a hyperbolic tangent function.[37-38] The position of the interface also fluctuates; in the melt, the positional fluctuations relate to thermal fluctuations that produce random shifts in the position of each point of the BCP interface over time and are commonly described using a capillary wave model.[38-39] After quenching into the glassy regime, positional fluctuations are locked into the surface that describes the interface between the blocks. These positional fluctuations contribute to the roughness of DSA patterns.[14]

Quantitative analysis of the STEM tomography data allowed us to specify the positional fluctuation of the PS/P2VP interface as a function of depth in the film and the location of the interface with respect to the features of the underlying template. To quantify the positional fluctuation of the PS/P2VP interface, the center of the PS/P2VP interface was found using the canny edge detection algorithm[40] and the standard deviation, σ, of this line from a straight line along the *y* axis was calculated for each interface and in each *xy* slice of the tomographic reconstructed volume (Figure S8). Positional fluctuation measurements were performed in two P2VP-*b*-PS-*b*-P2VP representative films: DSA film on a templates with W=1.4 $L_{0,s}$, and DSA film on a template with W=0.8 $L_{0,s}$. It should be noted that the choice of magnification in the TEM that enables high resolution structural characterization also limits the field of view for fluctuation analysis. Nonetheless, with ~850 nm field of view in the *y* direction, and an estimated resolution of 0.5 nm, the BCP interface fluctuations could be reliably measured.

Positional fluctuation (σ) of P2VP-*b*-PS-*b*-P2VP DSA film on templates with W=1.4 $L_{0,s}$ as a function of depth are presented in Figure 4a. σ differed across the film's depth, with high value at the top of the film (1.4 ± 0.1 nm) and at the bottom of the film (1.5 ± 0.1 nm), and lower values at the middle of the film's thickness (1.1 ± 0.1 nm). All measurements are shown as average ± one standard deviation of the 80 PS/P2VP interface in the tomographic field of view. Additional discussion about the errors in the fluctuations measurements of tomographic data can be found in the supporting information. The change in positional fluctuations with depth can be

visually seen in the *xy* slices in Movie 2. $\sigma_{template}$, measured before photoresist removal using SEM imaging, was 1.1 ± 0.1 nm, and while these fluctuations have an effect on the BCP fluctuations,[41] they do not solely explain the high fluctuations observed at the bottom of the film.

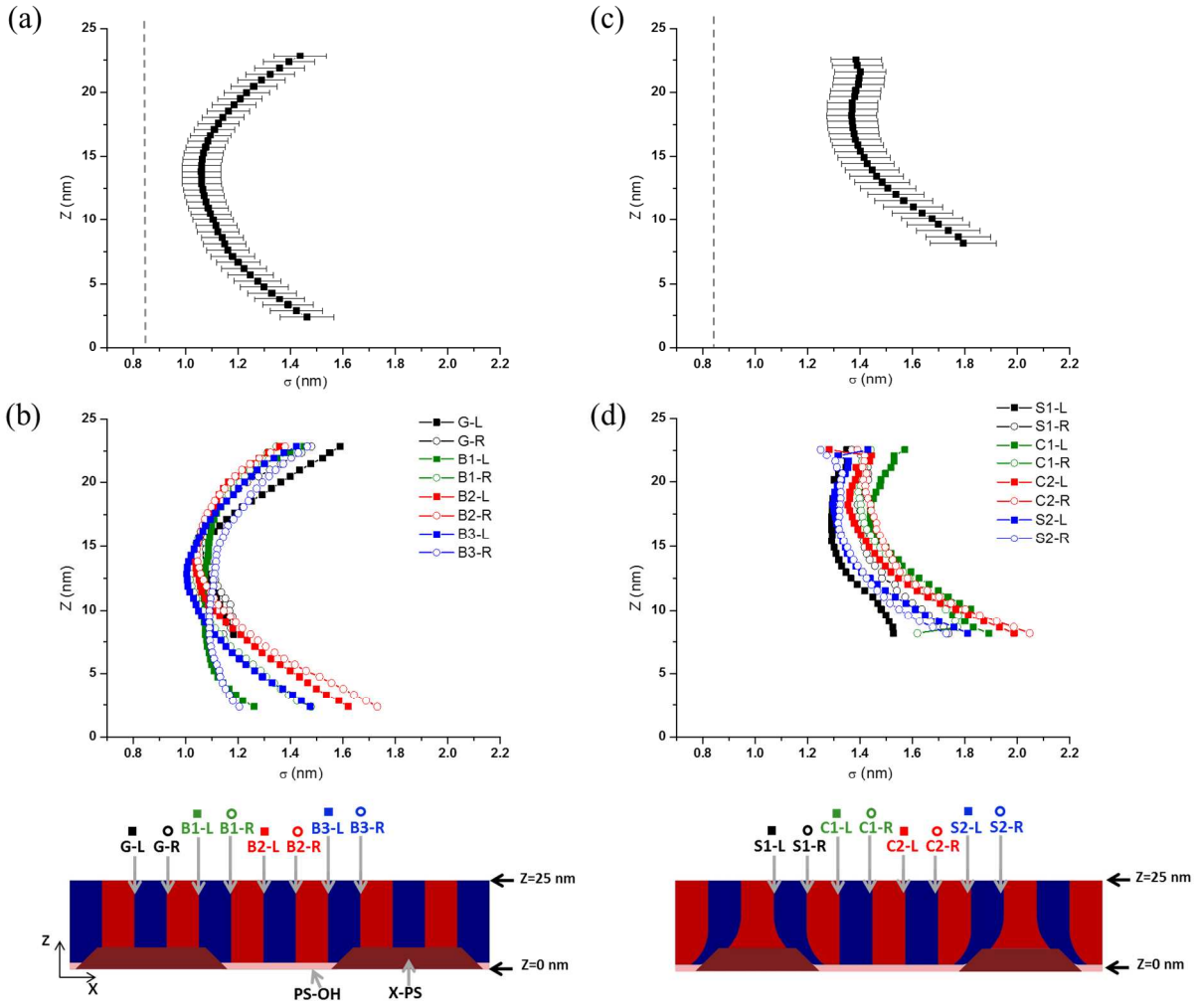

Figure 4: Positional fluctuation of the PS/P2VP interface as a function of depth in P2VP-*b*-PS-*b*-P2VP DSA film on templates with W=1.4 $L_{0,s}$ (a,b), and W=0.8 $L_{0,s}$ (c,d). (a,c) Average σ of all the interfaces measured in the tomographic reconstructed volume as a function of depth. The grey dashed line shows the theoretically predicted value of σ for P2VP-*b*-PS-*b*-P2VP (0.82 nm). (b,d) The fluctuations shown in (a) and (c) plotted per edge in the 4x density multiplication repeating unit, respectively. For each P2VP lamellae, the left edge is marked with solid squares, and the right edge is marked with open circles. Colors correspond to the lamellae location as depicted in the schematic illustrations at the bottom of the figure.

To gain insight into the origin of the depth-dependent behavior described previously, we compared the measured σ to the theoretically predicted value of P2VP-*b*-PS-*b*-P2VP fluctuations. The standard deviation of the interface position between polymer blocks can be predicated for a diblock system from the interface tension γ_0, the interfacial width, and the polymer periodicity L_0.[14, 37]

$$(1)\ \sigma^2 = \langle \delta_x{}^2 \rangle = \frac{1}{2\pi\gamma_0} \ln\left(\frac{L_0}{\Delta}\right)$$

where $\langle \delta_x{}^2 \rangle$ is the variance of the interface position between the polymer blocks. The interfacial width can be calculated using χ, the degree of polymerization *N*, and the statistical segment length a_{st}[14, 37]

$$(2)\ \Delta = 2a_{st} \frac{1}{(6\chi)^{0.5}} \left(1 + \frac{1.34}{(\chi N)^{\frac{1}{3}}}\right)$$

Although there has not been yet a theoretical description of the variance in interface position in triblock copolymers, theoretical calculations for diblock systems have been used for triblock copolymers by modifying the total degree of polymerization to N_{eff}, where $N_{eff} = N/2$.[42-43] The interface tension in equation (1) is calculated according to mean-field theory using the following equation (γ_0 is expressed in kT units):

$$(3)\ \gamma_0 = \frac{a_{st}\chi^{0.5}}{\upsilon 6^{0.5}}$$

where υ is the monomer volume.

In order to calculate the theoretical σ of PS/P2VP interface positional fluctuations, one must consider the effective χ of this system under SVA conditions. χ_{eff}, was calculated using equation 4:[26, 44]

$$(4)\ \chi_{eff} = \phi_p^{\alpha}\left(\frac{63}{T} - 0.033\right)$$

were ϕ_p is the polymer volume fraction in the solvated state, α is the power factor, and T is the annealing temperature in K. For the conditions used in this research, the polymer volume fraction in the solvated state (extracted from swelling ratio measurements) was 0.7, α was 1.6, and T was 298 K, resulting in χ_{eff}, of 0.101.

Using the values specified in Table 1, the theoretical σ of P2VP-*b*-PS-*b*-P2VP was calculated to be 0.83 nm. To compare this value to the measured σ as a function of depth in the DSA film, the theoretical value was plotted as a dashed grey line in Figure 4a. The comparison shows that in the middle of the film (10 nm < z < 15 nm), the positional fluctuations are closer to the theoretically predicted value than at the top and bottom of the film, suggesting that high fluctuations are suppressed by the neighboring polymer molecules. On the other hand, as P2VP-*b*-PS-*b*-P2VP gets closer to the interfaces it deviates from the predicted value and higher fluctuations are observed. We hypothesized that at the top and the bottom interfaces, the polymer molecules are more mobile and less constrained by the neighboring polymer molecules, resulting in higher fluctuations at the interfaces. Interfacial energy of the BCP- template can also play a role; at the BCP-template interface it is difficult to optimize the interfacial energy of the two blocks with the various regions of the template, leading to higher fluctuations at that interface.

Table 1: Characteristics of solvent annealed P2VP-*b*-PS-*b*-P2VP

Parameter	N	N_{eff}	χ_{eff}	$L_{0,s}$ (nm)[a]	a_{st} (nm)[45]	υ (nm^3)[28]
P2VP-*b*-PS-*b*-P2VP	450	225	0.101	21.0	0.67	0.18

a- Since the film was assembled on 84 nm pitch template with 4x density multiplication, $L_{0,s}$ of the DSA calculation was 21.0 nm

In order to understand the contribution of the various lamellae to the averaged σ in each *xy* slice, the PS/P2VP interface positional fluctuations were analyzed with respect to the position of the underlying template. The positional fluctuations of each of the eight interfaces present in the 4x density multiplication DSA film with W=1.4 $L_{0,s}$ are plotted as function of depth in Figure 4b. To ease the interpretation of the plot, errors bars were not included in this plot; we estimated the error as ± 0.1 nm. This individual interface investigation revealed an interesting phenomenon: while at the top two thirds of the film only minor differences are seen between the various interfaces, at the bottom third of the film, and in particular in z heights lower than the X-PS guiding stripe, there is a strong correlation between σ and the location of the interface, with symmetric behavior around the central $P2VP_B$ lamella (B2). The two PS/P2VP interfaces of the central $P2VP_B$ lamella (B2-L and B2-R, solid red squares and open red circles, respectively) have the highest standard deviation, reaching values of 1.6-1.7 nm close to the BCP-template interface. The two PS/P2VP interfaces adjacent to the central $P2VP_B$ lamella, B1-R and B3-L

(open green circles and solid blue squares, respectively), show almost identical positional fluctuations with intermediate σ value of 1.5 nm close to the BCP-template interface, while the two PS/P2VP interfaces that are the furthest away from the central $P2VP_B$ lamella (or closest to the guiding stripe), B1-L and B3-R (solid green squares and open blue circles, respectively), have the lowest σ values close to the BCP-template interface (1.2-1.3 nm). We interpret this behavior as related to the energy cost of positional fluctuations for the various interfaces. B1 and B3 (the left and right interfaces of $P2VP_B$) assemble on regions in the template which are preferential to one domain, in this case, the P2VP preferential guiding stripes sidewalls. High fluctuations of those interfaces will lead to frequent presence of P2VP or the neighboring PS on template sections that have different preference, which is unfavorable energetically. Thus, high positional fluctuations are suppressed in PS/P2VP adjunct to the guide stripes. B2, on the other hand, assembles solely on the brush in the template, which is considered non-preferential; thus, even when the B2 PS/P2VP interfaces wiggle, P2VP stays on the same brush region and higher fluctuations can be tolerated. The difference in positional fluctuation levels between the various P2VP lamellae can be seen directly in the *xy* slice at z ≈ 5 nm (Figure 2c, central column).

When P2VP-*b*-PS-*b*-P2VP was assembled on templates with W = 0.8 $L_{0,s}$, higher σ values were measured (1.4–1.8 nm, Figure 4c) compared to the assembly on W=1.4 $L_{0,s}$ (Figure 4a). The σ values were almost constant at the top 10 nm of the film, and then rapidly increased with depth to a maximum of 1.8 ± 0.1 nm at z = 8 nm. Positional fluctuations were not measured at smaller z due to the abundance of defects at the bottom of the film. The PS/P2VP interface positional fluctuations at the top of the film (1.4 ± 0.1 nm, Figure 4c) are very close to the values measured at the top of the film assembled on W=1.4 $L_{0,s}$ (1.4 ± 0.1, Figure 4a), suggesting a uniform behavior of assembly at the free surface. The high positional fluctuations observed z< 15 nm were attributed to the curvature in $P2VP_s$, and the abundance of defects formed at the bottom of this film.

In General, all the individual PS/P2VP interfaces showed similar trend with depth (Figure 4c). While the differences between the different PS/P2VP interfaces were small, the interfaces adjacent to the guide stripes (S1-L and S2-R; solid black squares and open blue circles, respectively) had consistently lower standard deviation values than the interfaces of the central lamellae (C1-L, C1-R, C2-L, and C2-R; solid green squares, open green circles, solid red

squares, and open red circles, respectively). It should be noted that measurements in *xy* slices can overestimate the fluctuation in curved lamellae since the positional fluctuations are normal to the interface surface while the measurements are done in slices parallel to the substrate. Thus, close to the guide stripes, $P2VP_S$ fluctuations have probably smaller values.

Current routine measurements of BCP DSA positional fluctuations (or line edge roughness) are preformed using top-down SEM images of the film, usually after etching one of the BCP domains to obtain high contrast imaging.[15-16, 41] The tomographic characterization, on the other hand, enabled us to probe the interface between the polymer blocks and through the depth of the film. The change in σ with depth and with relative position to the underlying template can have implications on understanding and designing BCP processes. First, the increase in fluctuations with distance from the guiding stripes at aligned DSA films (Figure 4b) suggest that while it is desirable to fabricate templates with large density multiplication factors, it might result in high positional fluctuations of lamellae that are far from the guiding stripes. Second, since minimal fluctuations were measured at the middle of the film thickness, we anticipate that in thicker DSA films, substantial part of the film thickness will have low fluctuations, which can still result to high fidelity structures after pattern transfer. Therefore, high aspect ratio DSA patterns might be preferable for obtaining low roughness. Third, techniques that probe structures in reciprocal space, such as X-ray scattering, often rely on models which describe the system as a single unit cell from one guiding stripe to another, exhibiting Gaussian fluctuations around the center of mass.[46] The fluctuations depth profile presented in this work implies that these models can be improved if the changes in positional fluctuations as a function of depth are accounted for.

The interfacial width of a BCP system plays an important role in the ability to transfer the BCP pattern to an underlying layer.[13] Measurements of the interface that probe the averaged structure, such as X-ray probes and neutron reflectivity, measure an "apparent" width Δ_a, which combines both the interfacial width and the positional fluctuations of this interface.[14, 16, 38] When the positional fluctuations follow a normal distribution, the relationship between Δ_a, Δ, and $\langle \delta_x{}^2 \rangle$ can be described using equation 5:[14, 37]

$$(5)\ \Delta^2 = \Delta_a^2 - 2\pi\langle \delta_x{}^2 \rangle$$

Tomographic characterization of DSA films provides a rare opportunity to extract the interfacial width from real space data since it enables examination of both the averaged structure and the positional fluctuation. Δ_a was measured from the averaged through-film structure while the fluctuations were measured in the *xy* slices. Since σ varied with depth and location, we focused our measurement and discussion on the middle of the film (z = 13.3 nm) of the best assembled sample (P2VP-*b*-PS-*b*-P2VP film on template with W = 1.4 $L_{0,s}$). At this z, the change in fluctuations with z was minimal and no distinctive difference between the various lamellae was found. Figure 5 shows the intensity profile (red circles) of the averaged cross section of P2VP-*b*-PS-*b*-P2VP DSA film on templates with W = 1.4 $L_{0,s}$ at z = 13.3 nm. Independent fitting of each lamella with a hyperbolic tangent function at both interfaces (blue line) resulted in an apparent width of Δ_a = 5.0 ± 0.4 nm. The fluctuations measured at that depth ($\sigma_{z=13.3nm}$ = 1.1 ± 0.1 nm; $\langle \delta_x^2 \rangle_{z=13.3nm}$ = 1.1 ± 0.1 nm^2) had a normal distribution and therefore can be used in equation (5), resulting in an interfacial width of Δ = 4.2 ± 0.4 nm. To compare the measured values with the predicted values of P2VP-*b*-PS-*b*-P2VP fluctuations, we turn back to equations (1) - (5). The predicted Δ and Δ_a, calculated from these equations and the parameters in Table 1, are 2.5 nm and 3.3 nm, respectively. The values determined from the TEM analysis are therefore significantly larger than the predicted values. TICG simulations predict an intermediate Δ_a value of 3.7 nm. The high apparent and interfacial width, measured from the tomographic data, hints that assembly in the solvated state and trapping that state during rapid drying in thin films leads to a PS/P2VP interfacial width understandably much broader than assembly without boundary conditions (thick film or bulk configuration). In previous studies on thermally annealed PS-PVP BCPs, interfacial widths of 2.8 nm to 3.3 nm were measured.[42, 47] Further study is needed to determine the relative contributions from SVA and other aspects of the DSA process to the apparent interfacial width. It should also be noted, that since the measurement was conducted on a stained film, there could be also an influence of the staining profile; while the iodine interacts with the pyridine group in the P2VP domain[32], small interaction with the PS domain could result in a wider measured apparent width. The contribution of various staining agents such as iodine and selective Al_2O_3 growth[19] to the interfacial profile measurements has not been quantified in past studies and is the subject of ongoing research.

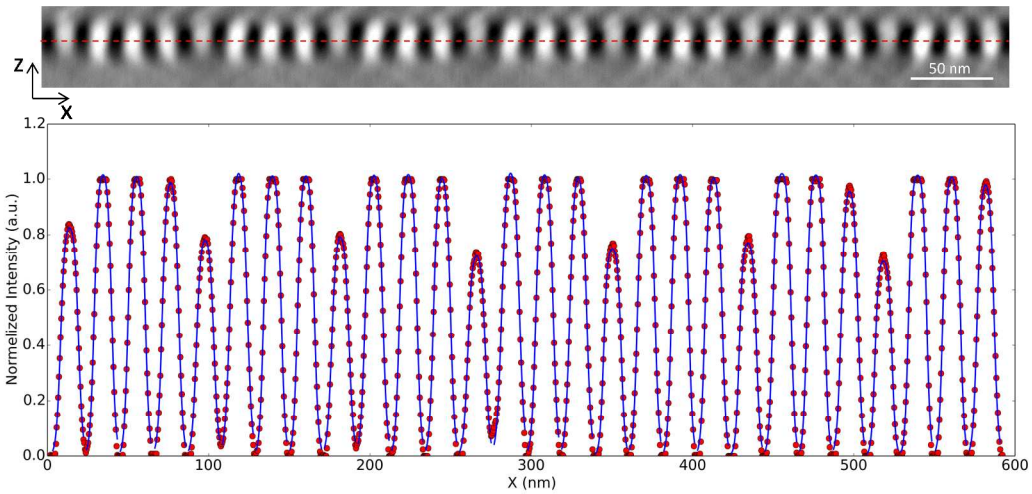

Figure 5: The apparent width of P2VP domains in P2VP-*b*-PS-*b*-P2VP DSA film on template with W=1.4 $L_{0,s}$. The intensity profile (red circles) of the averaged cross section at z = 13.3 nm (marked at the top with a dashed red line) was fitted with hyperbolic tangent function (blue line).

Understanding DSA defects

Understanding the origin of defects in BCP DSA films and the defects' morphology in the film is essential for developing processes with low defect density. The most common BCP-related defects in chemo-epitaxy DSA are: dislocations, residues with topography, micro-bridges, and line breakage.[12, 48] Recent investigations on the formation and kinetics of dislocations in DSA films have led to better understanding of their origin and 3D morphology.[9-10, 49] On micro-bridges and line breakage defects, on the other hand, little is known. In particular, there is scarce information on the formation of these defects in DSA films with density multiplication. Gronheid *et al.*[12] and Pathangi *et al.*[11] reported that micro-bridges (also called "flat bridges") are created in the BCP layer but are very difficult to detect after assembly and are usually identified only after the pattern transfer process.

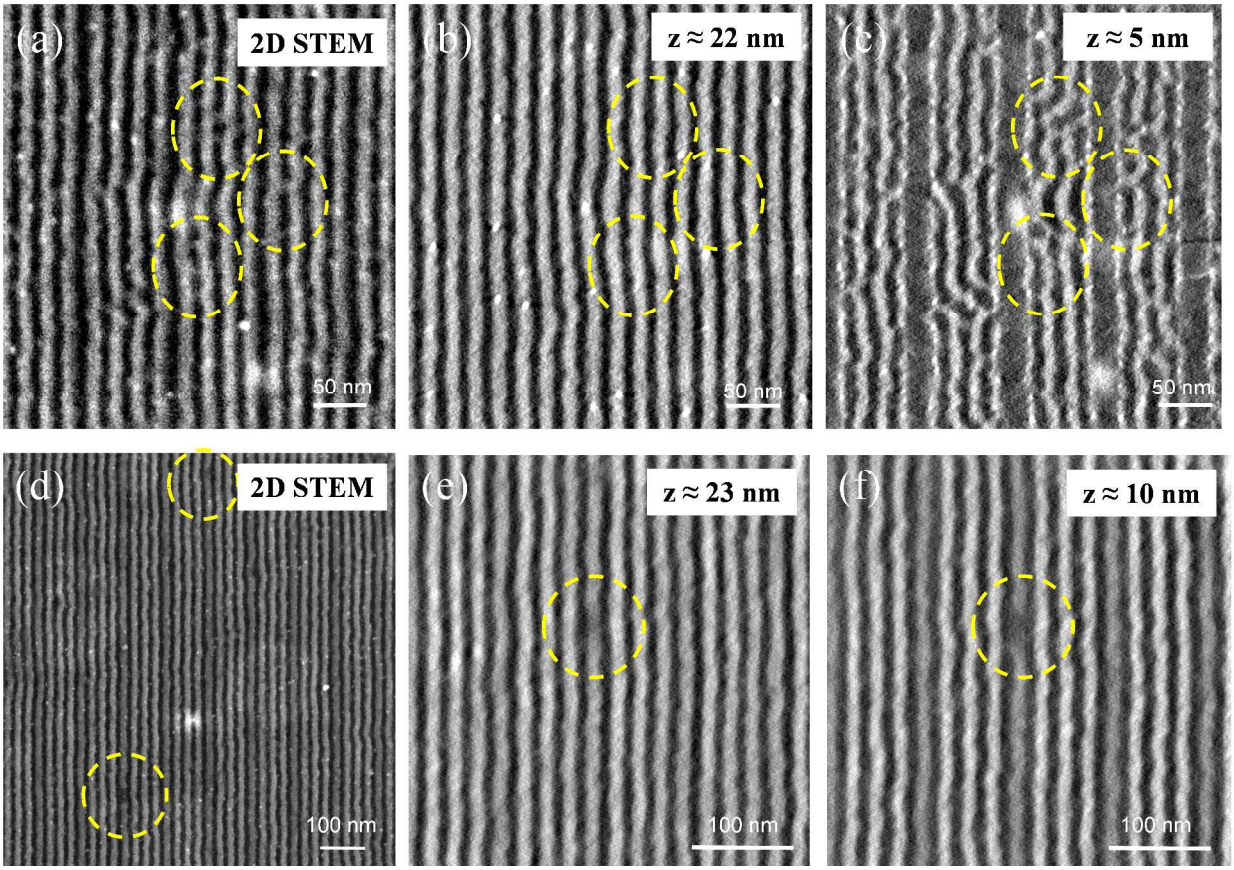

Figure 6: The three dimensional structure of DSA micro-bridge and line breakage defects. P2VP-*b*-PS-*b*-P2VP films were assembled on templates with (a-c) W = 0.8 $L_{0,s}$, or (d-f) W = 1.4 $L_{0,s0}$. (a) STEM image with few examples of defects that are classified as micro-bridge defects (marked with a dashed yellow circle). (b,c) *xy* slices from STEM tomography reconstruction volume of the same are shown in (a) at *z* heights 22 nm and 5 nm, respectively. (d) STEM image with two line breakage defects marked with dashed yellow circles. (e,f) *xy* slices from STEM tomography reconstruction volume of line breakage defect at *z* heights 23 nm and 10 nm, respectively.

In transmission microscopy, the 2D image is a projection of the 3D volume, similar to the effect of pattern transfer. By exploiting the abundance of defects in DSA film on templates with W=0.8 $L_{0,s}$, micro-bridges were explored. A 2D STEM image of P2VP-*b*-PS-*b*-P2VP DSA film on templates with W=0.8 $L_{0,s}$ (Figure 6a) shows several structures (marked with dashed yellow circles) that are reminiscent of the micro-bridges after pattern transfer. The *xy* slices obtained from STEM tomography reconstructed volume of the same area of Figure 6a reveal that one source for micro-bridges are defects that were formed at the bottom of the film (Figure 6c). These defects are not present at the top of the film (Figure 6b), and therefore cannot be identified using SEM characterization (Figure S6, supporting information). The defects persist through ~ 5

nm of the film thickness at the bottom of the film, and therefore can affect the quality of pattern transfer from this BCP film. While micro-bridge formations in the assembly investigated here is related to the non-optimal geometry of the template, it is reasonable to assume that other types of mismatch between the templates and the BCP will also lead to formation of micro-bridges defects. Indeed, Williamson *et al.* observed an increased formation of micro-bridges defects with an increased mismatch between the chemical composition of the BCP and the pre-pattern template (through BCP formulation).[30]

Line breakage defects were also observed in P2VP-*b*-PS-*b*-P2VP DSA (Figure 6d). These defects, found in P2VP-*b*-PS-*b*-P2VP DSA film on templates with W=1.4 $L_{0,s}$, are disconnected P2VP domains. Interestingly, they were found almost entirely in $P2VP_G$, *i.e.* on top of the X-PS guide stripe. STEM tomography of the defect reveals that the line breakage appears at the entire $P2VP_G$ thickness, with small disconnection at the top of the film (Figure 6e), and larger disconnection at the bottom of $P2VP_G$ (Figure 6f), close to the interface with the X-PS. We hypothesize that the line breakage defects are the result of defects in the X-PS guiding stripes (pinholes or local excess of X-PS), although accurate comparison between the templates and the BCP layer is needed in order to corroborate that.

Conclusions

Detailed investigation of the through-film structures, fluctuations, and defects in solvent annealed P2VP-*b*-PS-*b*-P2VP DSA films was conducted through STEM tomography three-dimensional characterization. The tomographic characterization together with molecular simulations enabled us to correlate between the template chemistry, geometry, and topography and the BCP assembled structure, and revealed hidden defects and curved lamellae at DSA films that were considered aligned from top-down imaging. The topography in the template together with preferential wetting of the X-PS side walls by the P2VP resulted in a side-wall driven directed assembly. Measurements of the positional fluctuations of the BCP domain interface, conducted through the film's depth and as function of the interface location in a density multiplication film, showed minimum fluctuations at the middle of the film thickness and an increase in fluctuations at the bottom of the film as PS/P2VP interfaces were further away from the guiding stripes. Moreover, it was demonstrated that combining positional fluctuations measurements and profile analysis of the through film averaged structure can enable interfacial

width measurements and shed light on BCP interface in a DSA processes. Finally, both micro-bridge defects and line breakage defects 3D structures were characterized, pinpointing the location of defects through the film's thickness and with regard to the pre-pattern template.

SVA and triblock DSA are examples of the growing arsenal of materials and processes that enable sub-10 nm DSA patterning;[26] this arsenal also includes top-coat DSA,[50] and high-χ, top-coat free materials.[51] While each method has specific parameters that influence the BCP assembly, in all these methods, the BCP interaction with the BCP-guiding pattern interface is crucial for successful directed assembly. Therefore, probing the BCP structure and its fluctuations at the BCP-guiding pattern interface is necessary to fully describe high χ DSA assembly, and enable better understanding of the assembly processes. Combining experimental observations of the BCP 3D structure with theoretical simulations will allow better design and implementation of BCP DSA.

Methods:

Materials: Poly(2-vinyl pyridine-*b*-styrene-*b*-2-vinyl pyridine) (P2VP-*b*-PS-*b*-P2VP) block copolymer (12k-*b*-23k-*b*-12k, PDI = 1.2) was purchased from Polymer Source and used as received. Cross linkable polystyrene (X-PS, AZEMBLY™ NLD128) was provided by AZ Electronic Materials and used as received. Hydroxyl-terminated poly styrene (PS-OH, M_n = 1.2 kg/mol) was purchased from Polymer Source and used as received. Silicon wafers (4", 200 µm thick, N-type, <100> orientation, double-side polished) coated with 30 nm-thick silicon nitride (SiN_x) on both sides were purchased from WRS Materials. GL-2000-12 e-beam resist was purchased from Gluonlab and was diluted with anisole v:v = 1:2.5. The solvents used in this research: toluene, acetone, anisole, and N-methyl-2-pyrrolidone (NMP), were purchased from Sigma-Aldrich and used as received. Iodine (I_2) was purchased from Sigma-Aldrich and used as received.

Sample preparation: 4" silicon wafers coated with SiN_x on both sides were used for sample fabrication. Using optical lithography and CF_4 plasma, 10 x 10 array of 1.3 mm x 0.5 mm rectangles with 3 mm spacing were patterned into the SiN_x on the back side of the wafer. The patterned SiN_x would later act as mask during KOH etching when the exposed silicon in the

rectangles would be removed to create windows for imaging. Following back side patterning, the wafer was cleaned with piranha solution, and then treated with oxygen plasma for 30 sec, to partially oxidize the front side SiN_x surface. Then, pre-pattern template was fabricated on the front side of the wafer according to the following procedure. A 7 nm X-PS mat was prepared by spin coating NLD128 at 1500 rpm and cross-linking at 270 °C for 30 min. 60 nm GL-2000 resist was coated and baked at 150 °C for 3 min. E-beam patterning was done on JEOL 9300 lithography system using 100 kV accelerating voltage, with varying dose, to create grating patterns consisting of parallel lines with pitch L_s = 84 nm (~$4L_{0,s}$ with slight polymer compression). The sample was developed in n-amyl acetate for 15 sec at room temperature. The pattern was then etched with oxygen plasma to break through the exposed X-PS mat as well as trimming the remaining resist and X-PS stripe to the desired width W. W of the X-PS guide stripes ranged from 15 to 40 nm, depending on the e-beam exposure dose. The resist was then removed with NMP and repeated sonication. PS-OH was coated at 1000 rpm and annealed at 200 °C for 1 hr to graft the brush to the exposed substrate between X-PS guide stripes. Ungrafted brush was then rinsed with NMP. 25 nm of P2VP-*b*-PS-*b*-P2VP was coated and annealed by solvent vapor annealing using acetone vapor for 1 hour. During the solvent-annealing, the swelling ratio of the polymer film was controlled by tuning the nitrogen flow through the SVA chamber, and was kept at 42% as determined by reflectometry (Filmetrics 60). After 1 hr, the SVA process was quenched by flowing nitrogen over the sample.

Following the DSA process, the wafer was back etched using KOH wet etch (30 wt % KOH, 85 °C, ~ 3 hr). With the front side of the wafer sealed and protected by a holder, the exposed silicon on the back side of the wafer was removed by KOH until the etching reached the silicon nitride on the front side, creating the imaging windows. The wafer was then cut up into individual windows for TEM imaging. Staining was conducted by exposing the samples to iodine vapors for 2 hours.

Imaging: STEM imaging and tomography was performed using a field-emission gun TEM operated at 200 kV, and camera length of 300 mm. For tomography, a series of STEM images were acquired at tilt angles ranging from -68° to +68° at angular interval of 3° from -54° to +54°, and at angular interval of 2° from +54° to +68° and from -54° to -68°. The morphology and feature sizes were unchanged after acquisition compared to the initial state and therefore the data

was not significantly affected by beam damage. The tilt series of the STEM images (51 projections) were aligned with Inspect 3D® software using iterative cross-correlations of the tilt series images. Iodine crystals (~2-3 nm in size) that accumulate on the bottom surface of the SiN_x window during the staining process and naturally occurring defects in the block copolymer film enhanced the accuracy of the cross-correlation. Reconstruction was performed using simultaneous iterative reconstruction technique (SIRT) algorithm applied through the same software. Segmentation (thresholding) of the reconstructed volume was performed using multi-thresholding in ImageJ to define the P2VP domains for surface rendering. Visualization of the segmented volume was performed using Avizo® software. z = 0 nm was defined where a significant loss of contrast and intensity occurred in the *xy* slice stack, and the *xy* slice series height was calculated using 0.47 nm z resolution. We estimate that there is a ± 0.47 nm error in determining the $z = 0$ height.

SEM imaging was performed using Zeiss Merlin field emission scanning electron microscope operating at 1 kV accelerating voltage. AFM measurements were performed on Bruker Multimode 5 AFM in tapping mode.

Quantitative image analysis:

For interfacial fluctuations measurements, in each *xy* slice the interface between the P2VP and PS was found using a canny edge detection routine.[40] Lines were fit to the edge pixels (using least squares) and the perpendicular distance from the edge pixel to the line was computed. The standard deviation of the distances between the individual edge locations and the fitted line was measured. For each lamella, over 1500 edge pixels were used in the computation of σ^2.

The apparent width (Δ_a) of the averaged cross section was measured for each lamella independently by fitting a hyperbolic tangent function with the intensity profiles in both sides:[38]

$$(6)\quad y = P1\left(\tanh\left(\frac{2(x-P2)}{\Delta_a}\right) - \tanh\left(\frac{2(x-P3)}{\Delta_a}\right)\right)$$

Where y is the normalized intensity of the image, x is the x coordinate of the pixel, and P1, P2, and P3 are parameters in the fit. The fitting was preform at z = 13.2 nm, where the interfacial fluctuations were relatively uniform with z. Since at this z there was no correlation between the lamellae population ($P2VP_G$, $P2VP_{B\text{-}R}$, $P2VP_{C\text{-}L}$, and $P2VP_{B\text{-}L}$) and the apparent width, the apparent width was averaged between all 28 lamellae that were measured.

Molecular simulations:

The P2VP-*b*-PS-*b*-P2VP system was modeled using a theoretically informed coarse grain Monte Carlo simulation with each polymer represented as a bead-spring chain. The system energy was defined according to the following Hamiltonian consisting of three separate parts: bonded-energy, non-bonded energy, and surface energy.

(7) $H = H_b + H_{nb} + H_s$

(8) $\frac{H_b}{k_B T} = \frac{3}{2}\sum_{i=1}^{n}\sum_{s=1}^{N}\frac{(N-1)|\boldsymbol{r}_i(s+1)-\boldsymbol{r}_i(s)|^2}{{R_e}^2}$

(9) $\frac{H_{nb}}{k_B T} = \sqrt{\bar{N}}\int_v \frac{d\boldsymbol{r}}{{R_e}^3}\left[\chi N\varphi_A\varphi_B + \frac{\kappa N}{2}(1-\varphi_A-\varphi_B)^2\right]$

(10) $\frac{H_s}{k_B T} = f_s\frac{\Lambda}{2d_s}\exp(-\frac{z^2}{2d_s^2})$

The bonded term describes the stretching between consecutive beads within the same chain. The non-bonded term accounts for the long range polymer-polymer interactions. The surface term describes the polymer interactions with the guiding stripe and side wall. In the bonded term, R_e is the root mean square end-to-end distance of the polymer chain, n is the number of chains in the simulation, and N is the number of beads per chain. In the non-bonded term, φ_A and φ_B are the normalized densities of PS and P2VP, respectively, χN is the Flory-Huggins interaction term, and κN is a compressibility term that penalizes deviations from the mean density. $\sqrt{\bar{N}}$, or the interdigitation number, is an estimate of the number of chains any given chain interacts with. In the surface energy term, f_s is either 1 or -1 depending on whether the surface is preferential or non-preferential to PS or P2VP, z is the distance from the nearest hard wall (guiding stripe, sidewall, or underlying substrate), Λ_s describes how strongly the surface interacts with the polymer, and d_s is the decay distance of the interaction. Random bead displacement and chain repetition moves were used to update the system according to the Metropolis Monte Carlo criteria in order to produce a system obeying the statistics of the NVT ensemble. The simulation was allowed to equilibrate over several thousand Monte Carlo turns until persistent structures had formed. Further details on how the simulation energies were calculated can be found in previous report.[34]

Each X-PS guiding stripe was represented by a trapezoid on an otherwise flat surface, where the sides of the trapezoid represent the guiding stripe side walls. Both the tops and side walls were

modeled as hard surfaces, and given independent $\Lambda_s N$ parameters for PS and P2VP. Simulation parameters were chosen for a P2VP-*b*-PS-*b*-P2VP symmetric triblock copolymer system with a pitch of 84 nm, periodicity of 21.3 nm, $\chi N = 55$, and film thickness of 25 nm. Guiding stripes had a height of 6.5 nm and sidewall angle of 23°, as depicted in Figure 1. Additionally, a neutral 2 nm thick brush was included. These parameters were chosen according to data collected on the templates using AFM, SEM, and spectroscopic elipsometry. The simulation box size was 252 nm X 84 nm X 25 nm (*x,y,z).* In order to reproduce the effects of solvent annealing, the simulation was first allowed to equilibrate under conditions near the order-disorder transition at $\chi N = 31$, giving rise to structures that would not be possible under the same conditions at larger χN. Once persistent equilibrium structures had formed at $\chi N = 31$, χN was ramped up to a final value of 55, which represents the conditions under which measurements would be taken. Structural and interfacial width data was collected once the structures had equilibrated at the final χN. Guiding stripe interaction parameters were chosen to reflect a three-tone pattern: the tops of the guiding stripes were made preferential to PS with $\Lambda_{top} N = -0.5$, while the sidewalls were made slightly preferential to P2VP with $\Lambda_{side} N = 1.0$; brush had a zero interaction term. A two-tone pattern was also simulated with both guiding stripe tops and sidewalls preferential to PS with $\Lambda_{top} N = \Lambda_{side} N = -0.5$.

Conflict of Interest: The authors declare no competing financial interest.

Acknowledgements

This work was supported in part by U.S. Department of Energy, Office of Science, Office of Basic Energy Sciences, at the Materials Science Division and at the Center for Nanoscale Materials, in Argonne National Laboratory under Contract No. DE-AC02-06CH11357. The project was in part funded by award 70NHNB14H012 from the U.S. Department of Commerce, National Institute of Standards and Technology, as part of the Center for Hierarchical Materials Design (CHiMaD). We gratefully acknowledge the computing resources provided on Blues, high-performance computing cluster operated by the Laboratory Computing Resource Center at Argonne National Laboratory. Tamar Segl-Peretz is a Horev Fellow, supported by the Taub Foundation.

Supporting Information Available: SEM image of AlO_x nanostructure templated by self-assembled P2VP-b-PS-b-P2VP, GISAXS scattering pattern of self-assembled P2VP-b-PS-b-P2VP, AFM measurement of X-PS guiding stripes, STEM tomography visualizations, 2D STEM images and SEM images of P2VP-b-PS-b-P2VP DSA film on various templates, molecular simulations of P2VP-*b*-PS-*b*-P2VP DSA film with different template-BCP interactions in three-tone geometry, edge detection of the tomographic data image, short discussion about the origin of errors in interfacial fluctuations measurements of tomographic data, and three movies of *xy* and *xz* slices of the tomographic data. These material are available free of charge *via* the Internet at http://pubs.acs.org.

References:

1. Dusa, M.; Quaedackers, J.; Larsen, O. F. A.; Meessen, J.; van der Heijden, E.; Dicker, G.; Wismans, O.; de Haas, P.; van Ingen Schenau, K.; Finders, J.; Vleeming, B.; Storms, G.; Jaenen, P.; Cheng, S.; Maenhoudt, M., Pitch Doubling Through Dual-Patterning Lithography Challenges in Integration and Litho Budgets. *Proc. SPIE* **2007**, *6520*, 65200G.
2. Xu, P.; Chen, Y.; Chen, Y.; Miao, L.; Sun, S.; Kim, S.-W.; Berger, A.; Mao, D.; Bencher, C.; Hung, R.; Ngai, C., Sidewall Spacer Quadruple Patterning for 15nm Half-Pitch. *Proc. SPIE* **2011**, *7973*, 79731Q.
3. Gregory, S. D.; He, G.; Lei, W.; Jeff, L.; Patel, K. C.; Yves-Andre, C.; Ricardo, R.; Thomas, R. A., Transfer of Self-Aligned Spacer Patterns for Single-Digit Nanofabrication. *Nanotechnology* **2015**, *26*, 085304.
4. Ouk Kim, S.; Solak, H. H.; Stoykovich, M. P.; Ferrier, N. J.; de Pablo, J. J.; Nealey, P. F., Epitaxial Self-Assembly of Block Copolymers on Lithographically Defined Nanopatterned Substrates. *Nature* **2003**, *424*, 411-414.
5. Bita, I.; Yang, J. K. W.; Jung, Y. S.; Ross, C. A.; Thomas, E. L.; Berggren, K. K., Graphoepitaxy of Self-Assembled Block Copolymers on Two-Dimensional Periodic Patterned Templates. *Science* **2008**, *321*, 939-943.
6. Ross, C. A.; Berggren, K. K.; Cheng, J. Y.; Jung, Y. S.; Chang, J.-B., Three-Dimensional Nanofabrication by Block Copolymer Self-Assembly. *Adv. Mater.* **2014**, *26*, 4386-4396.
7. Liu, C.-C.; Ramírez-Hernández, A.; Han, E.; Craig, G. S. W.; Tada, Y.; Yoshida, H.; Kang, H.; Ji, S.; Gopalan, P.; de Pablo, J. J.; Nealey, P. F., Chemical Patterns for Directed Self-Assembly of Lamellae-Forming Block Copolymers with Density Multiplication of Features. *Macromolecules* **2013**, *46*, 1415-1424.
8. Li, W.; Müller, M., Defects in the Self-Assembly of Block Copolymers and Their Relevance for Directed Self-Assembly. *Annu. Rev. Chem. Biomol. Eng.* **2015,** *6*, 187-216.
9. Hur, S.-M.; Thapar, V.; Ramírez-Hernández, A.; Khaira, G.; Segal-Peretz, T.; Rincon-Delgadillo, P. A.; Li, W.; Müller, M.; Nealey, P. F.; de Pablo, J. J., Molecular Pathways for Defect Annihilation in Directed Self-Assembly. *Proc. Natl. Acad. Sci.* **2015**, *112*, 14144-14149.
10. Kim, B.; Laachi, N.; Delaney, K. T.; Carilli, M.; Kramer, E. J.; Fredrickson, G. H., Thermodynamic and Kinetic Aspects of Defectivity in Directed Self-Assembly of Cylinder-Forming Diblock Copolymers in Laterally Confining Thin Channels. *J. Appl. Polym. Sci.* **2014**, *131*, 40790.
11. Pathangi, H.; Chan, B. T.; Bayana, H.; Vandenbroeck, N.; Van Den Heuvel, D.; Van Look, L.; Rincon-Delgadillo, P.; Cao, Y.; Kim, J.; Lin, G.; Parnell, D.; Nafus, K.; Harukawa, R.; Chikashi, I.; Nagaswami, V.; D'Urzo, L.; Gronheid, R.; Nealey, P., Defect Mitigation and Root Cause Studies in IMEC's 14 nm Half-Pitch Chemo-Epitaxy DSA Flow. *Proc. SPIE* **2015**, *9423*, 94230M.
12. Gronheid, R.; Rincon Delgadillo, P.; Pathangi, H.; Van den Heuvel, D.; Parnell, D.; Chan, B. T.; Lee, Y.-T.; Van Look, L.; Cao, Y.; Her, Y.; Lin, G.; Harukawa, R.; Nagaswami, V.; D'Urzo, L.; Somervell, M.; Nealey, P., Defect Reduction and Defect Stability in IMEC's 14 nm half-pitch Chemo-Epitaxy DSA Flow. *Proc. SPIE* **2014**, *9049*, 904905.
13. Wan, L.; Ruiz, R.; Gao, H.; Patel, K. C.; Albrecht, T. R.; Yin, J.; Kim, J.; Cao, Y.; Lin, G., The Limits of Lamellae-Forming PS-*b*-PMMA Block Copolymers for Lithography. *ACS Nano* **2015**, *9*, 7506-7514.

14. Stein, G. E.; Liddle, J. A.; Aquila, A. L.; Gullikson, E. M., Measuring the Structure of Epitaxially Assembled Block Copolymer Domains with Soft X-ray Diffraction. *Macromolecules* **2010**, *43*, 433-441.

15. Sunday, D. F.; Ashley, E.; Wan, L.; Patel, K. C.; Ruiz, R.; Kline, R. J., Template–Polymer Commensurability and Directed Self-Assembly Block Copolymer Lithography. *J. Polym. Sci., Part B: Polym. Phys.* **2015**, *53*, 595-603.

16. Sunday, D. F.; Hammond, M. R.; Wang, C.; Wu, W.-l.; Delongchamp, D. M.; Tjio, M.; Cheng, J. Y.; Pitera, J. W.; Kline, R. J., Determination of the Internal Morphology of Nanostructures Patterned by Directed Self Assembly. *ACS Nano* **2014**, *8*, 8426–8437.

17. Segal-Peretz, T.; Winterstein, J.; Ren, J.; Biswas, M.; Liddle, J. A.; Elam, J. W.; Ocola, L. E.; Divan, R. N. S.; Zaluzec, N.; Nealey, P. F., Metrology of DSA Process Using TEM Tomography. *Proc. SPIE* **2015**, 9424, 94240U.

18. Gotrik, K. W.; Lam, T.; Hannon, A. F.; Bai, W.; Ding, Y.; Winterstein, J.; Alexander-Katz, A.; Liddle, J. A.; Ross, C. A., 3D TEM Tomography of Templated Bilayer Films of Block Copolymers. *Adv. Funct. Mater.* **2014**, *24*, 7689-7697.

19. Segal-Peretz, T.; Winterstein, J.; Doxastakis, M.; Ramírez-Hernández, A.; Biswas, M.; Ren, J.; Suh, H. S.; Darling, S. B.; Liddle, J. A.; Elam, J. W.; de Pablo, J. J.; Zaluzec, N. J.; Nealey, P. F., Characterizing the Three-Dimensional Structure of Block Copolymers *via* Sequential Infiltration Synthesis and Scanning Transmission Electron Tomography. *ACS Nano* **2015**, *9*, 5333-5347.

20. Hur, S.-M.; Khaira, G. S.; Ramírez-Hernández, A.; Müller, M.; Nealey, P. F.; de Pablo, J. J., Simulation of Defect Reduction in Block Copolymer Thin Films by Solvent Annealing. *ACS Macro Lett.* **2015**, *4*, 11-15.

21. Sun, Z.; Chen, Z.; Zhang, W.; Choi, J.; Huang, C.; Jeong, G.; Coughlin, E. B.; Hsu, Y.; Yang, X.; Lee, K. Y.; Kuo, D. S.; Xiao, S.; Russell, T. P., Directed Self-Assembly of Poly(2-vinylpyridine)-*b*-polystyrene-*b*-poly(2-vinylpyridine) Triblock Copolymer with Sub-15 nm Spacing Line Patterns Using a Nanoimprinted Photoresist Template. *Adv. Mater.* **2015**, *27*, 4364-4370.

22. Chaudhari, A.; Ghoshal, T.; Shaw, M. T.; Cummins, C.; Borah, D.; Holmes, J. D.; Morris, M. A., Formation of Sub-7 nm Feature Size PS-*b*-P4VP Block Copolymer Structures by Solvent Vapour Process. *Proc. SPIE* **2014**, *9051*, 905110.

23. Kim, J. M.; Kim, Y.; Park, W. I.; Hur, Y. H.; Jeong, J. W.; Sim, D. M.; Baek, K. M.; Lee, J. H.; Kim, M.-J.; Jung, Y. S., Eliminating the Trade-Off between the Throughput and Pattern Quality of Sub-15 nm Directed Self-Assembly *via* Warm Solvent Annealing. *Adv. Funct. Mater.* **2015**, *25*, 306-315.

24. Nealey, P. F.; Wan, L. Solvent Annealing Block Copolymers on Patterned Substrates. US20120202017 A1, Aug. 9, **2012**.

25. Wan, L.; Ji, S.; Liu, C.-C.; Craig, G. S. W.; Nealey, P. F., Directed Self-Assembly of Solvent-Vapor-Induced Non-Bulk Block Copolymer Morphologies on Nanopatterned Substrates. *Soft Matter* **2016**, *12*, 2914-2922.

26. Xiong, S.; Wan, L.; Ishida, Y.; Chapuis, Y.-A.; Craig, G. S. W.; Ruiz, R.; Nealey, P. F., Directed Self-Assembly of Triblock Copolymer on Chemical Patterns for Sub-10-nm Nanofabrication *via* Solvent Annealing. *ACS Nano* **2016**, 10, 7855–7865

27. Dai, K. H.; Kramer, E. J., Determining the Temperature-Dependent Flory Interaction Parameter for Strongly Immiscible Polymers From Block Copolymer Segregation Measurements. *Polymer* **1994**, *35*, 157-161.
28. Eitouni, H.; Balsara, N., Thermodynamics of Polymer Blends. In *Physical Properties of Polymers Handbook*, Mark, J., Ed. Springer New York: **2007**; pp 339-356.
29. Yoshida, H.; Suh, H. S.; Ramirez-Herunandez, A.; Lee, J. I.; Aida, K.; Wan, L.; Ishida, Y.; Tada, Y.; Ruiz, R.; de Pablo, J.; Nealey, P. F., Topcoat Approaches for Directed Self-Assembly of Strongly Segregating Block Copolymer Thin Films. *J. Photopolym. Sci. Technol.* **2013**, *26*, 55-58.
30. Williamson, L. D.; Seidel, R. N.; Chen, X.; Suh, H. S.; Rincon Delgadillo, P.; Gronheid, R.; Nealey, P. F., Three-Tone Chemical Patterns for Block Copolymer Directed Self-Assembly. *ACS Appl. Mater. Interfaces* **2016**, *8*, 2704-2712.
31. Paik, M. Y.; Bosworth, J. K.; Smilges, D.-M.; Schwartz, E. L.; Andre, X.; Ober, C. K., Reversible Morphology Control in Block Copolymer Films *via* Solvent Vapor Processing: An *in Situ* GISAXS Study. *Macromolecules* **2010**, *43*, 4253-4260.
32. Sawyer, L. C. G., David T. , *Polymer Microscopy*. Springer Science: **1996**.
33. Delgadillo, P. A. R. Origin of defects in directed self-assembly of diblock copolymers using feature multiplications. Ph.D. Dissertation, Univeristy of Chicago, Chicago, IL, and KU Leuven, Belgium, **2014**.
34. Detcheverry, F. A.; Kang, H.; Daoulas, K. C.; Müller, M.; Nealey, P. F.; de Pablo, J. J., Monte Carlo Simulations of a Coarse Grain Model for Block Copolymers and Nanocomposites. *Macromolecules* **2008**, *41*, 4989-5001.
35. Liu, C.-C.; Han, E.; Onses, M. S.; Thode, C. J.; Ji, S.; Gopalan, P.; Nealey, P. F., Fabrication of Lithographically Defined Chemically Patterned Polymer Brushes and Mats. *Macromolecules* **2011**, *44*, 1876-1885.
36. Cushen, J. D.; Wan, L.; Blachut, G.; Maher, M. J.; Albrecht, T. R.; Ellison, C. J.; Willson, C. G.; Ruiz, R., Double-Patterned Sidewall Directed Self-Assembly and Pattern Transfer of Sub-10 nm PTMSS-*b*-PMOST. *ACS Appl. Mater. Interfaces* **2015**, *7*, 13476–13483.
37. Semenov, A. N., Theory of Block Copolymer Interfaces in the Strong Segregation Limit. *Macromolecules* **1993**, *26*, 6617-6621.
38. Shull, K. R.; Mayes, A. M.; Russell, T. P., Segment Distributions in Lamellar Diblock Copolymers. *Macromolecules* **1993**, *26*, 3929-3936.
39. Matsen, M. W., The Standard Gaussian Model for Block Copolymer Melts. *Journal of Physics: Condensed Matter* **2002**, *14*, R21.
40. Canny, J., A Computational Approach to Edge Detection. *Pattern Analysis and Machine Intelligence, IEEE Transactions* **1986**, *PAMI-8*, 679-698.
41. Stoykovich, M. P.; Daoulas, K. C.; Müller, M.; Kang, H.; de Pablo, J. J.; Nealey, P. F., Remediation of Line Edge Roughness in Chemical Nanopatterns by the Directed Assembly of Overlying Block Copolymer Films. *Macromolecules* **2010**, *43*, 2334-2342.
42. Anastasiadis, S. H.; Retsos, H.; Toprakcioglu, C.; Menelle, A.; Hadziioannou, G., On the Interfacial Width in Triblock *versus* Diblock Copolymers: A Neutron Reflectivity Investigation. *Macromolecules* **1998**, *31*, 6600-6604.
43. Matsen, M. W.; Thompson, R. B., Equilibrium Behavior of Symmetric ABA Triblock Copolymer Melts. *J. Chem. Phys.* **1999**, *111*, 7139-7146.
44. Lodge, T. P.; Hanley, K. J.; Pudil, B.; Alahapperuma, V., Phase Behavior of Block Copolymers in a Neutral Solvent. *Macromolecules* **2003**, *36*, 816-822.

45. Hiemenz, P. C.; Lodge, T., *Polymer chemistry*. 2nd ed.; CRC Press: Boca Raton, **2007**; pp 587.
46. Guinier, A., *X-ray Diffraction in Crystals, Imperfect Crystals, and Amorphous Bodies*. Dover: **1994**.
47. Koneripalli, N.; Levicky, R.; Bates, F. S.; Matsen, M. W.; Satija, S. K.; Ankner, J.; Kaiser, H., Ordering in Blends of Diblock Copolymers. *Macromolecules* **1998**, *31*, 3498-3508.
48. Bencher, C.; Smith, J.; Miao, L.; Cai, C.; Chen, Y.; Cheng, J. Y.; Sanders, D. P.; Tjio, M.; Truong, H. D.; Holmes, S.; Hinsberg, W. D., Self-Assembly Patterning for Sub-15 nm Half-Pitch: a Transition From Lab to Fab. *Proc. SPIE* **2011**, *7970*, 79700F.
49. Nagpal, U.; Müller, M.; Nealey, P. F.; de Pablo, J. J., Free Energy of Defects in Ordered Assemblies of Block Copolymer Domains. *ACS Macro Lett.* **2012**, *1*, 418-422.
50. Bates, C. M.; Seshimo, T.; Maher, M. J.; Durand, W. J.; Cushen, J. D.; Dean, L. M.; Blachut, G.; Ellison, C. J.; Willson, C. G., Polarity-Switching Top Coats Enable Orientation of Sub–10-nm Block Copolymer Domains. *Science* **2012**, *338*, 775-779.
51. Hirahara, E.; Paunescu, M.; Polishchuk, O.; Jeong, E.; Ng, E.; Shan, J.; Kim, J.; Hong, S.; Baskaran, D.; Lin, G.; Vora, A.; Tjio, M.; Arellano, N.; Rettner, C. T.; Lofano, E.; Liu, C.-C.; Tsai, H.; Chunder, A.; Nguyen, K.; Friz, A. M.; Bowers, A. N.; Balakrishnan, S.; Cheng, J. Y.; Sanders, D. P. Directed Self-Assembly of Topcoat-Free, Integration-Friendly High-X Block Copolymers, *Proc. SPIE* **2015,** 9425, 94250P.